nature.com   Publications A-Z index   Browse by subject   Welcome back Stijn Mertens   Cart   Stijn Mertens   Logout

Current Issue   Volume 534   Issue 7609

CURRENT ISSUE

目次 | العربية

About the cover

THIS WEEK
Editorials
World View
Research Highlights
Seven Days

NEWS IN FOCUS
News
Features

COMMENT
Comment
Books and Arts
Correspondence
Obituary

CAREERS
Column

Futures

RESEARCH
News & Views
Perspectives
Articles
Letters

The sum of 390 sequential 1-MB photographs of an aqueous electrolyte drop in motion across a switchable boron nitride surface. Stiction, or static friction, is the force required to persuade an object to start sliding across a surface. It is technologically important in devices with moving parts in contact, but is not well understood. Stijn Mertens *et al*. describe an inorganic model system for the study of the relationships between surface wetting, stiction, adhesion and lubrication. The system is a hexagonal boron nitride monolayer that can be electrochemically switched by intercalation of hydrogen between a corrugated and a flat morphology. The change in the surface structure of the boron nitride alters the adhesion and its balance with stiction of an aqueous drop sliding across the monolayer. The work of adhesion increases in going from the flat to the corrugated surface, whereas the stiction threshold does not change significantly. Thus the authors make a quantitative connection between the macroscopic properties of stiction and adhesion as a result of structural control at the atomic scale.

Previous issue

LETTER

Switching stiction and adhesion of a liquid on a solid

Stijn F. L. Mertens[1,2]*, Adrian Hemmi[3]*, Stefan Muff[3], Oliver Gröning[4], Steven De Feyter[1], Jürg Osterwalder[3] & Thomas Greber[3]

When a gecko moves on a ceiling it makes use of adhesion and stiction. Stiction—static friction—is experienced on microscopic and macroscopic scales and is related to adhesion and sliding friction[1]. Although important for most locomotive processes, the concepts of adhesion, stiction and sliding friction are often only empirically correlated. A more detailed understanding of these concepts will, for example, help to improve the design of increasingly smaller devices such as micro- and nanoelectromechanical switches[2]. Here we show how stiction and adhesion are related for a liquid drop on a hexagonal boron nitride monolayer on rhodium[3], by measuring dynamic contact angles in two distinct states of the solid–liquid interface: a corrugated state in the absence of hydrogen intercalation and an intercalation-induced flat state. Stiction and adhesion can be reversibly switched by applying different electrochemical potentials to the sample, causing atomic hydrogen to be intercalated or not. We ascribe the change in adhesion to a change in lateral electric field of in-plane two-nanometre dipole rings[4], because it cannot be explained by the change in surface roughness known from the Wenzel model[5]. Although the change in adhesion can be calculated for the system we study[6], it is not yet possible to determine the stiction at such a solid–liquid interface using *ab initio* methods. The inorganic hybrid of hexagonal boron nitride and rhodium is very stable and represents a new class of switchable surfaces with the potential for application in the study of adhesion, friction and lubrication.

Every object at rest sticks with some adhesion to its substrate. If this object is moved, then a force must act on it. This force has to overcome the stiction threshold, above which the object starts to move and below which it sticks to the substrate. This fundamentally simple principle indicates a relationship between adhesion and stiction that is valid for a range of length scales from single-atom manipulation[7] up to the everyday experience of moving ourselves. Stiction is also related to sliding friction[1,8] and surface diffusion[9]. Empirically, these properties are connected via dimensionless coefficients that relate, for example, the diffusion barrier to the adsorption energy or the sliding friction force to the load. The advent of single-atom probes on surfaces and the measurement of the heat of adsorption have made the Evans–Polanyi relation, which postulates proportionality between the activation energy for diffusion and the adsorption energy, experimentally accessible[10]. For macroscopic objects, on the other hand, Amontons' first law, which states that sliding friction is proportional to the load, is much more complex because of the many length scales involved. This complexity also applies to stiction and, consequently, an *ab initio* understanding is difficult[11]. For such problems we rely on clear-cut responsive-surface model systems to study the influence of microscopic effects on their macroscopic expressions and vice versa.

For responsive surfaces, a collective change of a microscopic atomic or molecular parameter triggers a macroscopic property change such as the wetting angle of a liquid; such surfaces are central to nanoscience and smart-materials research[12–14]. Typically, the responsiveness is invoked by a change of conformation or charge state of organic molecules at the solid–liquid interface, which can be triggered by light[12], temperature[13] or electric fields[14]. The organic molecules at the basis of the switching, however, render these surfaces quite fragile and limited to near-ambient temperatures. By contrast, the inorganic hexagonal boron nitride/rhodium (h-BN/Rh) hybrid we focus on has very high thermal and chemical stability (see Methods), and therefore signifies a class of responsive surfaces with considerable technological promise. The stability of the h-BN/Rh system is related to the covalently bonded network of the h-BN 'skin' in comparison with the weaker supramolecular interactions in self-assembled monolayers.

The boron nitride nanomesh is a corrugated monolayer of h-BN on rhodium[3,15]: 13×13 h-BN units form a superhoneycomb structure on 12×12 Rh(111) unit cells, in which particularly strong lateral electric fields exist that are, for instance, decisive for the self-assembly of molecules[4]. The nanomesh structure is stable in vacuum up to 1,000 °C and survives immersion into liquids[4,16]. In ultrahigh vacuum, it was found that the boron nitride layer could be made flat by intercalation of atomic hydrogen[17]. Here, we demonstrate this effect under electrochemical conditions and show that h-BN/Rh(111) is a surface with switchable wetting and adhesion.

The electrochemical switching of the surface texture is based on intercalation of atomic hydrogen, as is demonstrated in Fig. 1. Figure 1a shows cyclic voltammograms for a clean Rh(111) film and a h-BN nanomesh sample in perchloric acid solution in a sessile drop configuration[18]. In the negative scan direction, the Rh(111) reference voltammogram exhibits the typical atomic hydrogen adsorption peak just before the onset of molecular hydrogen evolution[19]. On h-BN/Rh(111), this peak occurs at less negative potentials, which suggests that the process is energetically slightly more favourable on the nanomesh. During the reverse scan, the single desorption peak on Rh(111) shows a double peak for h-BN/Rh(111), which indicates a two-stage desorption process. Integration of the hydrogen adsorption peak yields $75\,\mu\text{C cm}^{-2}$, which amounts to one-third of the bare Rh(111) measurement where one monolayer of hydrogen may be adsorbed, and confirms earlier observations[16,17]. On continued cycling (Fig. 1b), a slight sharpening of the adsorption peak occurs; the charge related to the peak integral changes by less than 15%, demonstrating the stability of the h-BN overlayer upon cycling.

The changes in nanotexture that accompany the hydrogen adsorption and desorption were visualized directly by *in situ* electrochemical scanning tunnelling microscopy (EC-STM). Figure 1c–f shows the same area for different substrate potentials. Initially, at potential E_1 (Fig. 1c), the hexagonal pattern of pores separated by wires is observed[16,17]. The 3.2-nm periodicity can also be seen in the autocorrelation of a given section from one terrace, and the corrugation is reflected by the root-mean-square (r.m.s.) roughness. Crossing of the hydrogen adsorption peak (potential E_2, Fig. 1d) leads to flattening of the surface, which is reflected in the vanishing of the superstructure and a decrease in the r.m.s. roughness. A tip change between Fig. 1c and Fig. 1e caused a contrast inversion of the pore, which, however, does not affect the r.m.s. analysis. When the potential is set back to

[1]Department of Chemistry, KU Leuven, Celestijnenlaan 200F, 3001 Leuven, Belgium. [2]Institut für Angewandte Physik, Technische Universität Wien, Wiedner Hauptstrasse 8–10/E134, 1040 Wien, Austria. [3]Physik-Institut, Universität Zürich, Winterthurerstrasse 190, 8057 Zürich, Switzerland. [4]Empa, Swiss Federal Laboratories for Materials Science and Technology, Überlandstrasse 129, 8600 Dübendorf, Switzerland.
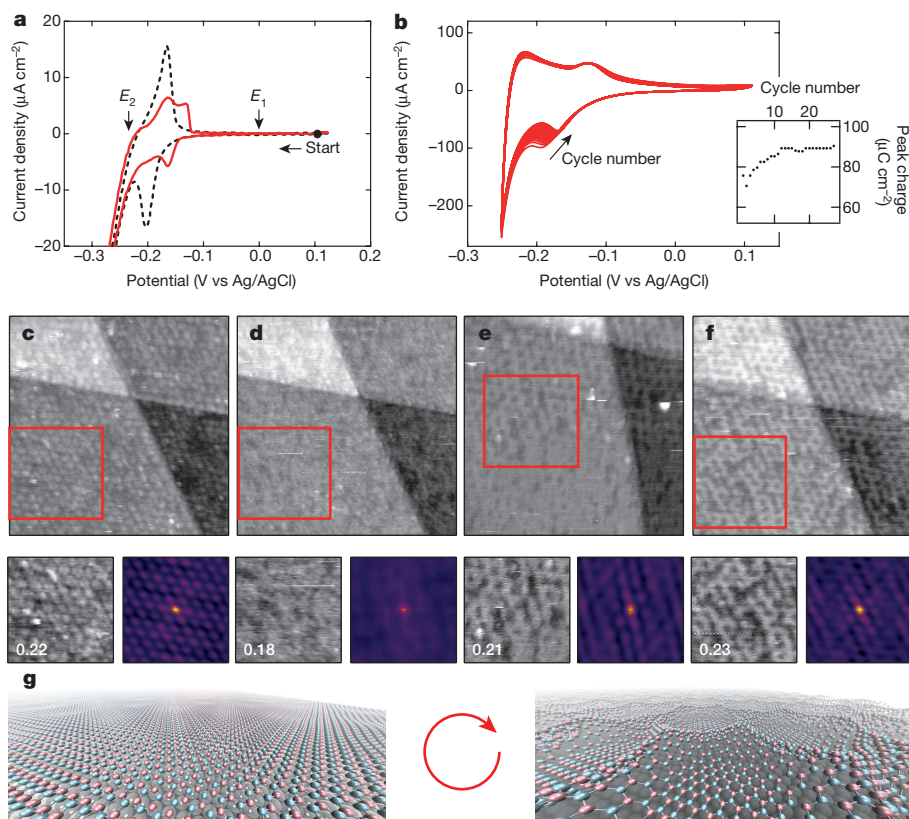*These authors contributed equally to this work.

Figure 1 | Voltammetry and electrochemical scanning tunnelling microscopy. a, Cyclic voltammogram of h-BN nanomesh on Rh(111) (red trace) and of Rh(111) (black dashed trace) in contact with a sessile drop of 0.1 M $HClO_4$. Scan rate, 1 mV s^{-1}. The hydrogen adsorption peak is found at -150 mV for h-BN/Rh(111) and at -200 mV for Rh(111). $E_1 = 0$ V and $E_2 = -0.25$ V are the substrate potentials at which *in situ* STM was performed. **b**, Stability of the hydrogen adsorption/desorption peaks over multiple cycles (28 cycles shown, recorded in a standard electrochemical cell; scan rate, 10 mV s^{-1}). The charge of the hydrogen adsorption peak as a function of cycle number is shown in the inset. **c–f**, Sequence of *in situ* STM images for a region with three atomic terrace levels, at various substrate potentials: $E_1 = 0$ V (**c**); $E_2 = -0.25$ V (**d**); switching $E_2 \rightarrow E_1$ (**e**; image scanned from bottom to top); and $E_1 = 0$ V after recovery of corrugation (**f**). The red square highlights the same area of the sample in all panels; close-ups (1.2 × magnification) are shown in the bottom-left panels. The white numbers are the r.m.s. roughness in units of the terrace height. The bottom-right panels show the autocorrelations of the bottom-left panels and reveal, if present, the 3.2-nm periodicity of the h-BN superstructure. Image sizes, 66 nm × 66 nm; tunnelling current, 0.1 nA; tip potential fixed at -0.45 V. **g**, Three-dimensional representation of the flat (left) and the corrugated h-BN layer (right). N, sky blue; B, pink; Rh, dark grey; H, white. For clarity, the heights of N and B above the Rh top layer have been stretched by a factor of three. Coordinates taken from refs 17 and 29.

the initial value, the corrugation gradually reappears (Fig. 1e), which indicates that deintercalation is slower than the forward process (see Methods and Extended Data Fig. 2). After the cycle (Fig. 1f), the superhoneycomb shows different imperfections (for example, some pores appear connected). The physical picture that emerges is illustrated in Fig. 1g: electrochemical intercalation of hydrogen reversibly flattens the h-BN/Rh nanomesh, and in doing so switches off the dipole rings in the surface.

To prove unequivocally that hydrogen intercalation is at the basis of the observed switching effect, we conducted an ambient-to-vacuum transfer experiment with the goal of quantifying the intercalated hydrogen. The electrochemical treatment was performed in heavy water, and the h-BN/Rh(111) sample was extracted from the solution under potential control and transferred in less than 10 min to vacuum (see Methods) where thermal desorption spectroscopy (TDS) was carried out, as shown in Fig. 2. Deuterium desorption from the sample held at potential E_2 (flat state) is obvious, whereas no substantial desorption took place from a sample that was kept at E_1 (corrugated) throughout. The desorption temperature indicates slightly higher binding energy as compared to hydrogen on bare Rh(111) (ref. 20). This further confirms hydrogen intercalation, because hydrogen (or deuterium) on top of h-BN would not bind as strongly as on rhodium and would not survive the transfer from the liquid to the vacuum. Our experiments do not show atomistic details of the way in which the hydrogen intercalates, although it has been claimed[21] that protons can pass through an intact h-BN layer, and that this process is facilitated by the presence of a platinum group metal (see Methods). In this scenario, the hydrated protons in the liquid electrolyte are probably stripped of their solvation shell the instant intercalation occurs, or a Grotthuss-type transport mechanism may be involved[22].

Stiction of the electrolyte on the h-BN surface is studied by measuring dynamic contact angles, which differ from the equilibrium value

in Young's equation. This difference can be directly observed if a liquid drop on a solid loses volume by evaporation, where the drop footprint will start to move only below a critical contact angle (the receding angle). Likewise, when the volume of the drop is gradually increased, the footprint moves when the advancing contact angle is reached[23,24]. The difference in advancing and receding angles and the concomitant contact angle hysteresis are a macroscopic expression of adhesion and stiction. In Fig. 3, we show dynamic contact angle measurements for
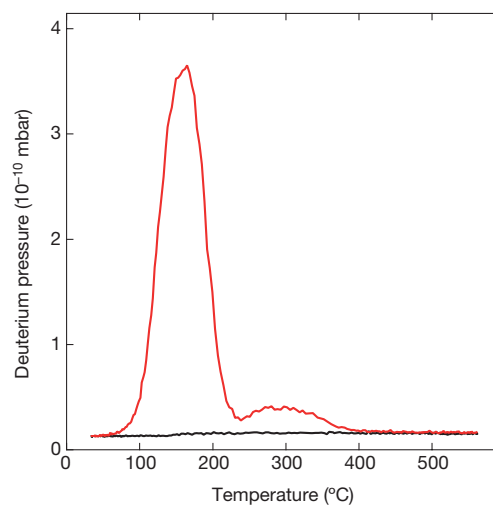

Figure 2 | Deuterium thermal desorption spectra. h-BN/Rh(111) was exposed to 0.1 M $DClO_4$ in D_2O at substrate potentials of $E_1 = 0$ V (black trace) and $E_2 = -0.25$ V (red trace). After loading the samples in the electrolyte they were transferred to ultrahigh vacuum for TDS (see Methods). Heating rate, 0.9 K s^{-1}.
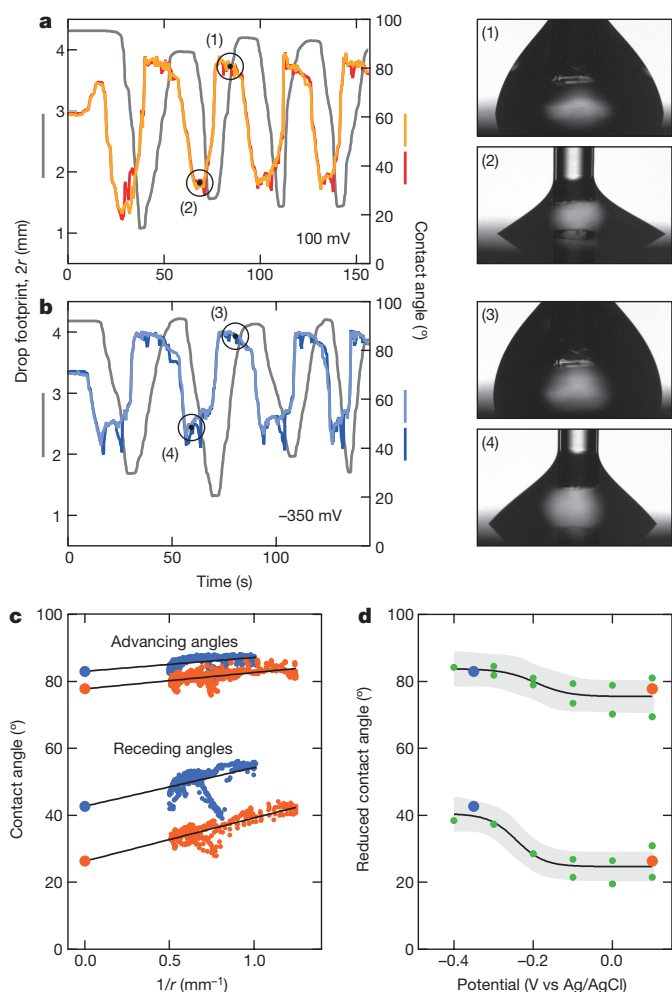
Figure 3 | Dynamic contact angle measurements. a, Left (orange) and right (red) contact angles (right axis) and drop footprints (with diameters of $2r$; grey, left axis) as functions of time. Pictures of an advancing (1) and a receding (2) drop in the transients at 100 mV (corrugated state; indicated by the circled points in the left panel) are shown on the right. **b**, Left (dark blue) and right (light blue) contact angles and drop footprints as functions of time. Pictures of an advancing (3) and receding (4) drop in the transients at −350 mV (flat state; indicated by the circled points in the left panel) are shown on the right. **c**, Contact angles in **a** (100 mV, red) and **b** (−350 mV, blue) versus $1/r$ for times above 40 s. Extrapolation to $1/r = 0$ (infinite drop footprint) yields reduced contact angles that are independent of the contact line. **d**, Reduced receding (bottom) and advancing (top) angles for different applied potentials, where the hydrogen intercalation peak is found at about −0.2 V. The large red and blue points correspond to the values determined in **c**. The solid lines are sigmoid fits through all experimental points (green circles), from which values of θ_a and θ_r for the corrugated (76.0° ± 1.2° and 24.5° ± 1.4°, respectively) and the flat (84.3° ± 2.3° and 40.1° ± 3.2°, respectively) state are determined. The grey band indicates the 1-s.d. prediction interval.

Figure 4 | Wetting angle hysteresis and stiction. The footprint of a drop starts to move with an advancing (left; θ_a) or a receding (right; θ_r) angle, if the friction-induced lateral tension exceeds the stiction threshold γ_H. The equilibrium angle from Young's equation θ_0 lies between θ_a and θ_r. γ_S, γ_{LS} and γ_L are the corresponding solid–gas, liquid–solid and liquid–gas interface energies, respectively.

changes that are reproduced for subsequent cycles. All the effects due to residual imperfections, however, are distinct from the effect of the electrochemical potential. The size dependence of the wetting hysteresis is a consequence of the line tension, that is, the work required to change the length of the drop perimeter[25]. If the wetting angles are plotted against the inverse of the footprint radius (Fig. 3c), then the line tension and the extrapolation of the wetting angle for infinite footprints may be inferred. In Fig. 3d, these extrapolated advancing and receding angles are plotted for a large set of experiments as a function of the applied potential, correlating the applied substrate potential with the measured contact angles. Clearly, the hystereses for potentials above −200 mV are different from those below this threshold of the hydrogen adsorption peak. Further experiments indicate that neither visible evolution of molecular hydrogen (where the reduction current increases exponentially in the voltammogram) nor electrowetting effects[26,27] can be responsible for the observed changes in contact angle.

The concept for stiction and the concomitant contact angle hysteresis is sketched in Fig. 4: the static friction σ balances the forces that distort the Young equilibrium $\gamma_S - \gamma_{LS} - \gamma_L \cos(\theta_0) = 0$ (in which γ_S, γ_{LS} and γ_L are the interfacial energies or tensions of the solid–gas, liquid–solid and gas–liquid interfaces, and θ_0 is the Young equilibrium angle). The static friction σ acts parallel to the surface, as do γ_S and γ_{LS}, and invokes a new equilibrium angle θ_σ. The new equilibrium angle is determined by

$$\gamma_S - \gamma_{LS} - \gamma_L \cos(\theta_\sigma) + \sigma = 0$$

The static friction σ may, however, not exceed a critical value $\pm \gamma_H$, above which the footprint of the drop starts to move with an advancing or a receding angle. In Fig. 3c, d, the size-independent receding and advancing angles (that is, the extrapolation to infinite footprints) θ_r and θ_a are indicated for the corrugated and the flat h-BN layer. Their values are given by

$$\cos(\theta_{r,a}) = \cos(\theta_0) \mp \frac{\gamma_H}{\gamma_L}$$

in which $\gamma_H \geq \sigma$ is the stiction threshold. With the knowledge of γ_L (72 mJ m^{-2} for water), which does not depend on the surface of the solid, and the determination of θ_a and θ_r, γ_H and θ_0 may be directly determined.

Our experiments indicate that the hydrogen-intercalation-induced flattening of the h-BN nanomesh increases θ_0 from 54.9° ± 0.8° to 64.5° ± 1.7°. Using the Young–Dupré equation we determine the work of adhesion per unit area w_{LS} from γ_L and the Young equilibrium angle θ_0 (ref. 28):

$$w_{LS} = \gamma_L + \gamma_S - \gamma_{LS} = \gamma_L[1 + \cos(\theta_0)]$$

The work of adhesion decreases from $(1.58 \pm 0.01)\gamma_L$ by 9.2% ± 1.8% in going from the corrugated to the flat layer. The stiction threshold γ_H of $(0.33 \pm 0.01)\gamma_L$ and $(0.33 \pm 0.03)\gamma_L$ for corrugated and flat layers,

applied potentials around the hydrogen adsorption peak. The angles as determined from inflating and deflating the drops in the corresponding videos (Supplementary Videos 1, 2) are shown for a potential above (Fig. 3a) and below (Fig. 3b) the hydrogen peak, that is, for the corrugated and the flat surface, respectively. The drop volume was changed periodically and distinct receding angles θ_r and advancing angles θ_a were observed. Four positions are shown as photographs of the electrolyte drop on a h-BN/Rh(111) sample with the capillary, which is 0.85 mm in diameter, entering the drop from the top. The experiments show distinct hysteresis in the contact angles of about 60°. The observed angles also depend on residual defects, which is reflected in the asymmetry between the left and the right footprint, and in sudden angle
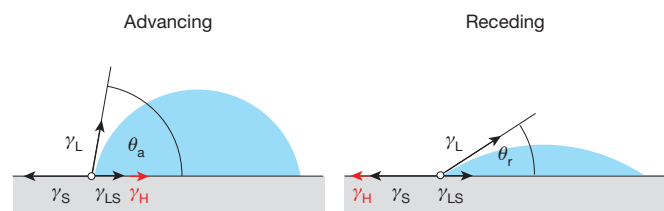
respectively, is (within the error bars) the same for the two interfaces. The change in work of adhesion is incompatible with a Wenzel model[5], according to which a change in effective surface area is responsible for a change in wetting angle: the effective surface area of the corrugated h-BN is 3% or 0.5% larger than that of the flat layer if a calculated corrugation height of 316 pm (ref. 29) or 83 pm (ref. 17) is used. Thus, to explain the magnitude of the change in adsorption energy, an electronic effect must amplify the change induced by the corrugation. We argue that this electronic effect is due to the loss of the lateral electric fields (2-nm dipole rings)[4] in the hydrogen-intercalated surface. The ratio of adsorption energies can be tested by comparing them to water adsorption[30]. Taking the calculated adsorption energies of water[31] for different adsorption sites within the h-BN/Rh(111) supercell, we calculate the average adsorption energies of the corrugated and the flat state. If we take for the corrugated case the portion of the wire, pore (hole) and rim regions from Xe-adsorption[4], and set the flat state equivalent to the unfavourable adsorption on the wires, then we find an average adsorption energy that is 18% lower for water monomers and 9% lower for hexamers on intercalated h-BN compared to the h-BN nanomesh. The comparison to the experiment is much better for hexamers, which makes sense because hexamers represent the simplest possible 'drop' in which only every second water molecule makes a hydrogen bond to the boron nitride[30]. Beyond these estimations of the adsorption energies involved in the switching phenomenon, the comprehensively characterized structure of the nanomesh makes this surface very attractive for full-scale theoretical treatments of wetting, which is difficult for less ordered systems. Molecular dynamics results estimate a change in adhesion (adsorption energy) of 4% (ref. 6), which compares favourably with the 9.2% extracted from our wetting angle data; however, a quantitative theoretical description of stiction is still a distant prospect.

We have presented a switchable surface on which macroscopic static friction and adhesion can be linked to our understanding of water adsorption on this surface at the microscopic scale. The relatively simple structure of the h-BN nanomesh makes it amenable to accurate descriptions down to the atomic level, and an attractive model system for full-scale theoretical analyses of switchable surfaces, wetting, friction and lubrication. The fact that the intercalated surface survives emersion from the electrolyte could make this test system widely applicable for the study of friction and lubrication, even if the adhering objects differ from liquid drops. In a biological context, it might be possible to create complex multi-cellular arrangements by influencing cell migration through controlled switching between high and low adhesiveness to cells. In the context of technological advancement, the high thermal and chemical stability of the system means it could be used even in harsh environments, for example, to influence capillary action, stiction and adhesion in microfluidic or nanoelectromechanical devices. Finally, beyond the field of adhesion and friction, electrochemical hydrogen intercalation may be used to obtain freestanding boron nitride layers or, more exotically, to stably confine tritium beneath a maximally transparent single-atomic-layer moderator, as is needed to determine the neutrino mass through β-decay spectroscopy[32].

Online Content Methods, along with any additional Extended Data display items and Source Data, are available in the online version of the paper; references unique to these sections appear only in the online paper.

Received 10 August 2015; accepted 12 April 2016.

1. Persson, B. N. J. *Sliding Friction* (Springer, 1998).
2. Wagner, T. J. W. & Vella, D. Switch on, switch off: stiction in nanoelectromechanical switches. *Nanotechnology* **24,** 275501 (2013).
3. Corso, M. *et al.* Boron nitride nanomesh. *Science* **303,** 217–220 (2004).
4. Dil, H. *et al.* Surface trapping of atoms and molecules with dipole rings. *Science* **319,** 1824–1826 (2008).
5. Wenzel, R. N. Surface roughness and contact angle. *J. Phys. Chem.* **53,** 1466–1467 (1949).
6. Golze, D., Hutter, J. & Iannuzzi, M. Wetting of water on hexagonal boron nitride@Rh(111): a QM/MM model based on atomic charges derived for nanostructured substrates. *Phys. Chem. Chem. Phys.* **17,** 14307–14316 (2015).
7. Ternes, M., Lutz, C. P., Hirjibehedin, C. F., Giessibl, F. J. & Heinrich, A. J. The force needed to move an atom on a surface. *Science* **319,** 1066–1069 (2008).
8. Krim, J., Solina, D. H. & Chiarello, R. Nanotribology of a Kr monolayer: a quartz crystal microbalance study of atomic-scale friction. *Phys. Rev. Lett.* **66,** 181–184 (1991).
9. Ehrlich, G. & Hudda, F. Atomic view of surface self-diffusion: tungsten on tungsten. *J. Chem. Phys.* **44,** 1039–1049 (1966).
10. Evans, M. G. & Polanyi, M. Inertia and driving force of chemical reactions. *Trans. Faraday Soc.* **34,** 11–24 (1938).
11. Zhang, Q., Qi, Y., Hector, L. G. Jr, Cagin, T. & Goddard, W. A. III. Origin of static friction and its relationship to adhesion at the atomic scale. *Phys. Rev. B* **75,** 144114 (2007).
12. Ichimura, K., Oh, S.-K. & Nakagawa, M. Light-driven motion of liquids on a photoresponsive surface. *Science* **288,** 1624–1626 (2000).
13. Sun, T. *et al.* Reversible switching between superhydrophilicity and superhydrophobicity. *Angew. Chem. Int. Ed.* **43,** 357–360 (2004).
14. Lahann, J. *et al.* A reversibly switching surface. *Science* **299,** 371–374 (2003).
15. Berner, S. *et al.* Boron nitride nanomesh: functionality from a corrugated monolayer. *Angew. Chem. Int. Ed.* **46,** 5115–5119 (2007).
16. Widmer, R. *et al.* Electrolytic in situ STM investigation of h-BN-nanomesh. *Electrochem. Commun.* **9,** 2484–2488 (2007).
17. Brugger, T. *et al.* Nanotexture switching of single-layer hexagonal boron nitride on rhodium by intercalation of hydrogen atoms. *Angew. Chem. Int. Ed.* **49,** 6120–6124 (2010).
18. Willman, K. W. & Murray, R. W. Contact angle between water and a poly(vinylferrocene) film on a potential-controlled platinum electrode. *Anal. Chem.* **55,** 1139–1142 (1983).
19. Sung, Y. E., Thomas, S. & Wieckowski, A. Characterization of the Rh(111) electrode by CEELS, AES, LEED, and voltammetry. Adsorption of (bi)sulfate, perchlorate, and carbon monoxide. *J. Phys. Chem.* **99,** 13513–13521 (1995).
20. Colonell, J. I., Curtiss, T. J. & Sibener, S. J. Coverage dependence of the kinetics for H₂ desorption from Rh(111). *Surf. Sci.* **366,** 19–28 (1996).
21. Hu, S. *et al.* Proton transport through one-atom-thick crystals. *Nature* **516,** 227–230 (2014).
22. Marx, D., Tuckerman, M. E., Hutter, J. & Parrinello, M. The nature of the hydrated excess proton in water. *Nature* **397,** 601–604 (1999).
23. de Gennes, P. G. Wetting: statics and dynamics. *Rev. Mod. Phys.* **57,** 827–863 (1985).
24. Kwok, D. Y. & Neumann, A. W. Contact angle measurement and contact angle interpretation. *Adv. Colloid Interface Sci.* **81,** 167–249 (1999).
25. Amirfazli, A., Hanig, S., Müller, A. & Neumann, A. W. Measurements of line tension for solid–liquid–vapor systems using drop size dependence of contact angles and its correlation with solid–liquid interfacial tension. *Langmuir* **16,** 2024–2031 (2000).
26. Schneemilch, M., Welters, W. J. J., Hayes, R. A. & Ralston, J. Electrically induced changes in dynamic wettability. *Langmuir* **16,** 2924–2927 (2000).
27. Manukyan, G., Oh, J. M., van den Ende, D., Lammertink, R. G. H. & Mugele, F. Electrical switching of wetting states on superhydrophobic surfaces: a route towards reversible Cassie-to-Wenzel transitions. *Phys. Rev. Lett.* **106,** 014501 (2011).
28. Schrader, M. E. Young–Dupré revisited. *Langmuir* **11,** 3585–3589 (1995).
29. Iannuzzi, M. *et al.* Site-selective adsorption of phthalocyanine on h-BN/Rh(111) nanomesh. *Phys. Chem. Chem. Phys.* **16,** 12374–12384 (2014).
30. Ma, H. *et al.* Chiral distortion of confined ice oligomers (*n* = 5,6). *Langmuir* **28,** 15246–15250 (2012).
31. Ding, Y., Iannuzzi, M. & Hutter, J. Investigation of boron nitride nanomesh interacting with water. *J. Phys. Chem. C* **115,** 13685–13692 (2011).
32. Holzschuh, E., Fritschi, M. & Kündig, W. Measurement of the electron neutrino mass from tritium β-decay. *Phys. Lett. B* **287,** 381–388 (1992).

Author Contributions T.G. conceived the project together with S.F.L.M., who designed and performed the electrochemical experiments, *in situ* STM and *in situ* contact angle measurements. A.H. prepared the nanomesh samples, analysed contact angle data and performed the TDS measurements. S.M. built the contact angle apparatus. O.G. drew our attention to dynamic contact angle measurements. S.D.F. and J.O. managed the Sinergia project. All authors contributed to discussions. S.F.L.M., A.H. and T.G. prepared the manuscript.

Author Information Reprints and permissions information is available at www.nature.com/reprints. The authors declare no competing financial interests. Readers are welcome to comment on the online version of the paper. Correspondence and requests for materials should be addressed to S.F.L.M. (stmerten@gmail.com) or T.G. (greber@physik.uzh.ch).

METHODS

Experimental details. The experiments were performed in a clean room on single-layer h-BN grown on 150-nm-thick single-crystalline rhodium films on Si(111) wafers, which were protected with a 40-nm yttria-stabilized zirconia (YSZ) diffusion barrier[33]. The wetting angles were determined by a laboratory-built CCD camera set up to image at 15 frames per second and with an automated angle evaluation scheme (see Methods section 'Error analysis'). Electrochemical potential control was achieved using a Metrohm–Autolab PGSTAT101 potentiostat, using a laboratory-built glass syringe carrying a Ag/AgCl/3 M NaCl reference and Pt wire counter electrode. All electrochemical potentials are reported versus the Ag/AgCl reference. All glassware, including the glass capillary for *in situ* contact angle measurements, was cleaned by boiling in 20% nitric acid and rinsing with ultrapure water (MilliQ, Millipore, 18.2 MΩ cm), to ensure perfect wetting. The electrolyte was prepared from reagent-grade 70% HClO$_4$ (Sigma–Aldrich) and ultrapure water. For the deuterium desorption experiments, light water was replaced with D$_2$O (Fluka, D > 99.8%). All operations were carried out in an Ar-filled glove box in a clean room[33]. *In situ* STM was performed with an Agilent PicoLE system, using an electrochemically etched W tip that was coated with a thermoplastic polymer to minimize the faradaic current. The thermal desorption experiments were performed in an apparatus equipped with a calibrated quadrupole mass spectrometer (QMS 200 M2, Pfeiffer Vacuum), and pumped with a turbomolecular pump (TMU 071, Pfeiffer Vacuum)[17].

Thermal and chemical stability of the h-BN/Rh nanomesh. Experience in our laboratories since the discovery of the boron nitride nanomesh[3] indicates a shelf life of several years under ambient conditions, stability on exposure to, and ultrasonication in, common solvents (both polar and nonpolar), and after 15-min cycles in commercial UV–ozone cleaners. Furthermore, the nanomesh can be heated to 400 °C in air and close to 1,000 °C in vacuum[4]. By contrast, when exposed to hot, strongly alkaline solutions, the h-BN appears to be removed, in line with observations for bulk h-BN (ref. 34). Low-energy Ar$^+$ bombardment followed by annealing has been shown to produce atomically precise defects[35]. Hydrogen intercalation appears not to adversely affect the stability of the boron nitride layer[17]. As shown here, electrochemical cycling can be performed many times without signs of deterioration (Fig. 1b). Emersion of the intercalated sample and transfer to vacuum are possible and yield similar amounts of intercalated hydrogen as in an all-vacuum experiment (next section, Fig. 2 and ref. 17).

Adventitious adsorption from solution or the laboratory atmosphere was not observed, and attempts to adsorb organic molecules from solution were unsuccessful. These observations, together with the widely available cleaning methods listed above, make the nanomesh amenable to experiments under standard laboratory conditions.

Ambient-to-ultrahigh-vacuum transfer and TDS. A critical factor in our ambient-to-vacuum experiment is the successful emersion of the sample from the electrochemical environment, which means that potential control is required until the solid–bulk electrolyte interface ceases to exist. This way, the h-BN/Rh–electrolyte system is never allowed to assume its open circuit potential, where electrochemical deintercalation of the hydrogen may occur. This also explains why we can rinse the sample with ultrapure water to remove superficially adsorbed deuterium and traces of perchloric acid, before transferring the sample to vacuum. The successful extraction of the sample from the electrolyte is aided by its mild intrinsic hydrophobicity, akin to previous work[36] in which hydrophobic adlayers on noble metal electrodes after transfer to vacuum were studied.

The sample mounting and transfer into the vacuum chamber took about 10 min, during which the sample was exposed to water and ambient air. Because we expected that the remaining solvent molecules on the sample may still contribute to a deuterium signal during the desorption experiment, the sample was rinsed with ultrapure water after removal from the D$_2$O solution and before entry into the vacuum system. Artefacts from this procedure were excluded by comparing TDS spectra from two samples that were handled identically, but of which only one was held at the potential required for intercalation (see Fig. 2).

In the design of the sample holder, special precautions were taken to limit heating and desorption as much as possible to the sample itself, and to avoid a background covering the deuterium signal from the surface or risking the chamber pressure exceeding the safe operation limit of the mass spectrometer channel electron multiplier. To maximize the signal-to-noise ratio, heating should occur as locally and as fast as possible. Extended Data Fig. 1a shows the sample holders used, which allow the sample to be annealed via resistive heating solely through the 150-nm-thick Rh film[33]. In this configuration, only the top tungsten clamps became as hot as the sample and temperatures of 580 °C could be reached with a maximum pressure load of about 1.2×10^{-6} mbar. The sample configuration requires the use of a pyrometer to assess the sample temperature, which was

calibrated against a thermocouple reading of a Rh sample as shown in Extended Data Fig. 1b. Because the lowest measureable temperature by the pyrometer is around 350 °C, additional extrapolation of the curve sections outside this region was required.

Extended Data Fig. 1b displays all relevant information of a desorption experiment, such as the applied power to the sample, pyrometer, mass spectrometer and integral pressure readings. To determine the sample temperature, the following differential equations were used, which consider the power applied to the sample and its heat loss through radiation and thermal conduction to the sample holder:

$$\frac{dT}{dt} = aP(t) + bP(t)T(t) \qquad (1)$$

$$\frac{dT}{dt} = aP(t) + bT(t) \qquad (2)$$

with applied power P, sample temperature T, time t and fitting parameters a and b. Best results were obtained using equation (1) for the ascending temperature region and equation (2) for the descending temperature region of the heating/cooling curve. The extrapolated temperature was finally a complete numerical simulation of the temperature evolution, with room temperature as the starting point and the applied power being the only input variables.

Rate of hydrogen (de)intercalation. The hydrogen intercalation we study is closely related to underpotential deposition of hydrogen—that is, electrosorption at potentials positive from the hydrogen evolution equilibrium potential—which is known to occur on the platinum group metals[37], and to involve comparable energies on Pt and Rh[38,39]. As shown in Fig. 1a, hydrogen intercalation into h-BN/Rh occurs at a potential that is about 50 mV less negative than that for underpotential deposition of hydrogen on bare Rh(111), which may be due to the fact that intercalating hydrogen does not have to compete with ClO$_4^-$ for adsorption on Rh after passing the boron nitride overlayer[19].

From the *in situ* STM image in Fig. 1e, which was recorded immediately after switching the substrate potential from a value at which intercalated hydrogen is stable to a value at which electrochemical deintercalation takes place, it is apparent that recovery of the corrugation requires about half of the time taken to record one image. If the local corrugation is taken as a measure of deintercalation, then the line speed (8.1 lines per second) and image resolution (512 × 512 pixels) indicate a characteristic time of approximately 30 s. The forward process (intercalation) reproducibly led to a flattening in EC-STM in less than 1 s (Extended Data Fig. 2), indicating that intercalation is considerably faster than deintercalation. Restoration of the corrugation must be considered as the last step in the electrochemical deintercalation; it is not obvious which is the rate-determining process, to which the pore and wire areas of the nanomesh may contribute differently. The observed difference in the rate of intercalation and deintercalation may originate from unilateral catalytic activation by the Rh substrate[21]—that is, the different proton affinity of the h-BN/Rh and the h-BN/electrolyte interface—and is also convoluted with the kinetics of underpotential deposition of hydrogen[40].

Error analysis. The contact angles from one image frame are determined on the basis of fits of 32 sigmoid functions to the change in optical contrast for the left and right periphery of the drop, which are used to determine the location of the edge of the liquid drop. These fits, which are based on 60 raw data pixels, are all located in an interval of 0.25 mm centred at the footprint of the drop, and yield a fitting error for the edge location of about 0.8 μm. This error is five times less than the optical pixel width of the image and can be explained by the very sharp optical contrast between the background and the liquid drop. The angle is then fitted with two separate linear functions, one for the real edge between the background and the drop and one for its mirror image. The crossing of these two lines reveals the location of the footprint; the contact angle α is half the angle between the two fitted lines:

$$\alpha = 0.5[\arctan(|b_1|) + \arctan(|b_2|)] \qquad (3)$$

in which b_1 and b_2 are the slopes of the two linear fits (real angle and mirror angle). Equation (3) is valid for the left and right angles. Gaussian error propagation of equation (3) yields:

$$\Delta\alpha = \sqrt{\left(\frac{0.5\sigma b_1}{1 + b_1^2}\right)^2 + \left(\frac{0.5\sigma b_2}{1 + b_2^2}\right)^2}$$

in which σb_i is the error of the slope fits, and the accuracy of one measured contact angle is determined to be about 0.3°. For each extrapolation of the wetting angles
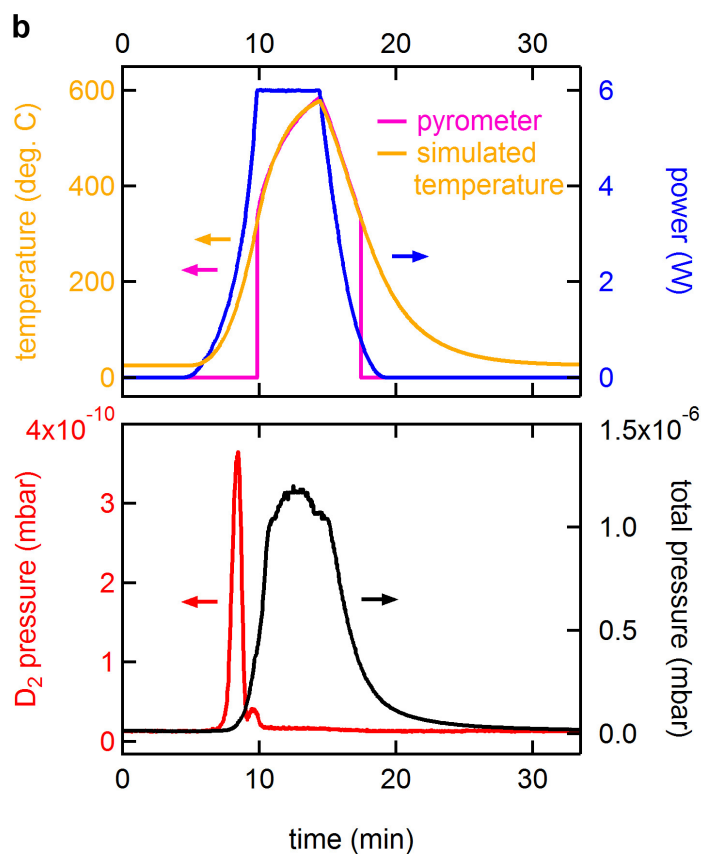
to $1/r = 0$, we used about 400 angles, which were determined using the procedure outlined above. The four linear fits shown in Fig. 3c are based on 412, 410, 344 and 402 individual angle data points, respectively from top to bottom. Because of the high accuracy and the large number of data points, we may neglect the error of the individual angles. The influence of, for example, residual defects, which induce asymmetries between the left and right angles and angle spikes (Fig. 3a–c), is visibly larger. The error of the reduced contact angle is the fitting error of the θ-axis intersection; the largest error for the datasets in Fig. 3c is 0.8°, which is well below the size of the printed dot.

In Fig. 3d we show all experiments and the corresponding advancing and receding angles performed on three different samples. The largest errors are not from the angle determination procedure described above, but mainly from differences between the samples, sample handling and manual operation of the syringe. The uncertainties that we cite are derived from the standard deviations of the mean values of the advancing and receding angles in Fig. 3d, where advancing and receding angles are taken from the sigmoid fits at the same applied potential. Values of θ_a and θ_r of 76.0° ± 1.2° and 24.5° ± 1.4°, respectively, for the corrugated and 84.3° ± 2.3° and 40.1° ± 3.2°, respectively, for the flat state are found. The values and error bars for θ_0, w_{LS} and γ_L are determined from the four angles and their standard deviations using Gaussian error propagation.

33. Hemmi, A. *et al.* High quality single atomic layer deposition of hexagonal boron nitride on single crystalline Rh(111) four-inch wafers. *Rev. Sci. Instrum.* **85,** 035101 (2014).
34. King, S. W., Nemanich, R. J. & Davis, R. F. Cleaning of pyrolytic hexagonal boron nitride surfaces. *Surf. Interface Anal.* **47,** 798–803 (2015).
35. Cun, H., Iannuzzi, M., Hemmi, A., Osterwalder, J. & Greber, T. Two-nanometer voids in single-layer hexagonal boron nitride: formation via the "can-opener" effect and annihilation by self-healing. *ACS Nano* **8,** 7423–7431 (2014).
36. Hansen, W. N. & Kolb, D. M. The work function of emersed electrodes. *J. Electroanal. Chem.* **100,** 493–500 (1979).
37. Koper, M. T. M. Blank voltammetry of hexagonal surfaces of Pt-group metal electrodes: comparison to density functional theory calculations and ultra-high vacuum experiments on water dissociation. *Electrochim. Acta* **56,** 10645–10651 (2011).
38. Jerkiewicz, G. & Zolfaghari, A. Determination of the energy of the metal–underpotential-deposited hydrogen bond for rhodium electrodes. *J. Phys. Chem.* **100,** 8454–8461 (1996).
39. Zolfaghari, A., Chayer, M. & Jerkiewicz, G. Energetics of the underpotential deposition of hydrogen on platinum electrodes. I. Absence of coadsorbed species. *J. Electrochem. Soc.* **144,** 3034–3041 (1997).
40. Łosiewicz, B., Jurczakowski, R. & Lasia, A. Kinetics of hydrogen underpotential deposition at polycrystalline rhodium in acidic solutions. *Electrochim. Acta* **56,** 5746–5753 (2011).

Extended Data Figure 1 | Thermal desorption spectroscopy. a, h-BN/Rh(111) thin-film sample and sample holder ready for the desorption experiment in the ultrahigh-vacuum chamber. **b**, Thermal desorption experiment with temperature and power data shown in the top panel and pressure data in the bottom panel. The purple data are pyrometer readings, which were calibrated to a previous thermocouple measurement using a Rh crystal. The simulated temperature is a solution of equations (1) and (2) with the applied power and a starting temperature of 25 °C as input variables.
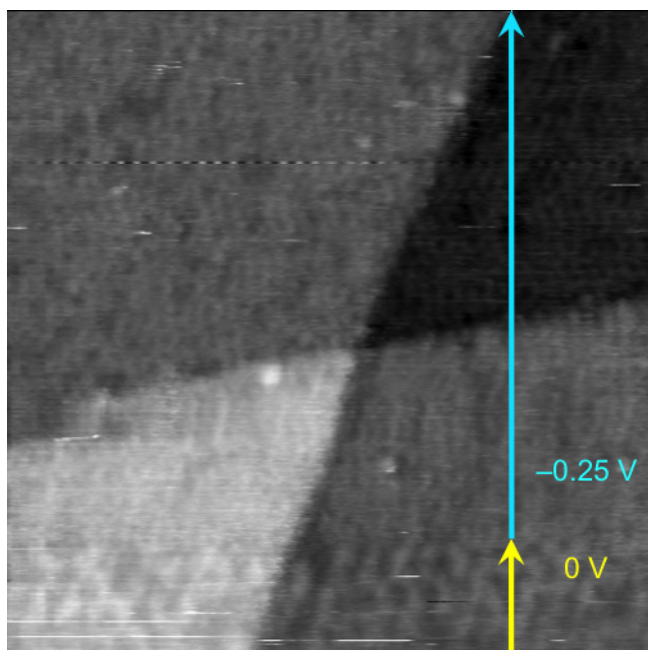
Extended Data Figure 2 | Electrochemical STM during hydrogen intercalation. The substrate potential during scanning (image scanned from bottom to top) was switched from $E_1 = 0\,V$ (deintercalated, yellow arrow) to $E_2 = -0.25\,V$ (intercalated, light blue arrow) at about one-fifth of the way from the lower edge of the STM image. On the timescale of imaging, intercalation-induced flattening of the surface is instantaneous, in sharp contrast to deintercalation (compare with Fig. 1e). Image size, 66 nm × 66 nm; tunnelling current, 0.1 nA; tip potential fixed at −0.45 V.